Surface-Enhanced Raman Scattering Holography

Matz Liebel[1*], Nicolas Pazos-Perez[2], Niek F. van Hulst[1,3*] and Ramon A. Alvarez-Puebla[2,3*]

[1] *ICFO-Institut de Ciencies Fotoniques, The Barcelona Institute of Science and Technology, 08860 Castelldefels, Barcelona, Spain*

[2] *Department of Physical and Inorganic Chemistry and EMaS, Universitat Rovira I Virgili, Carrer de Marcel.lí Domingo s/n, 43007 Tarragona, Spain*

[3] *ICREA, Passeig Lluís Companys 23, 08010 Barcelona, Spain*

*e-mails: Matz.Liebel@icfo.eu; Niek.vanHulst@icfo.eu; Ramon.Alvarez@urv.cat

ABSTRACT: Nanometric probes based on surface-enhanced Raman-scattering (SERS) are promising candidates for all-optical environmental, biological and technological sensing applications with intrinsic quantitative molecular specificity. However, the delicate conditions for effective SERS probes have so far hampered their wide application in SERS-imaging methodologies. In this article, we introduce holographic Raman microscopy, which allows single-shot 3D single particle localization and combine the imaging with novel bright nanoplasmonic superclusters that serve as a realistic test-system for future SERS sensing-probes. We validate our approach by simultaneously performing Fourier transform Raman spectroscopy of individual SERS nanoparticles, and Raman holography, using shearing interferometry to extract both the phase and the amplitude of wide-field Raman images, and ultimately 3D localise and track single SERS nanoparticles inside living cells. Our results pave the way towards multiplexed single-shot 3D concentration mapping in many different scenarios ranging from live cell and tissue interrogation to complex anti-counterfeiting applications.

During the last 40 years SERS spectroscopy[1–4] has emerged as a fast and reliable ultrasensitive technique for the confident and precise identification of molecular systems in a variety of complex samples[4–8]. Notwithstanding, to date, the major drawback is the low SERS efficiency and the resulting long acquisition times. State-of-the-art Raman spectrometers acquire spectra of complex plasmonic nanostructures within 100 ms. While this acquisition times may be more than enough for applications requiring single spectra acquisitions, such as the detection and/or quantification of biomolecules[9], toxic pollutants[10], explosives[11], or even microorganism[12] and cells[13], it completely hinders its applicability to other purposes, such as chemical imaging, where its prominent spatial resolution can excel. Unlike wide-field fluorescence microscopy, SERS imaging is still predominantly performed using scanning confocal microscopes. Thus, contrary to fluorescence where a snapshot image can be acquired in milliseconds to seconds, SERS imaging is registered serially point-by-point, increasing the acquisition times to hours[14,15]. In fact, this procedure not only restricts the area to be mapped, preventing 3D tomographic images, but also dramatically increases the damage of the mapped surface due to an excessive exposure to the excitation light. These two obstacles have prevented both potential applicability of SERS to the 3D imaging of living cells at the sub-cellular level, and technological applications, such as anti-counterfeiting.

Shortening of acquisition times requires the engineering of novel SERS particles designs with ultrabright response, together with alternative imaging spectroscopies for more effective data acquisition. In this article, we combine novel concepts in both directions. On the SERS particle side, plasmonic nanoparticle superclusters, obtained from small nanoparticle building blocks[16], are an ideal

particle-choice to generate very strong electric field in a restricted cluster size. The supercluster approach allows miniaturising the probe, thus increasing the spatial resolution, while simultaneously reducing negative impacts on cell viability[17]. On the imaging side, digital holography is an ideal candidate not only for volumetric imaging, but especially for the tracking of hundreds of individual particles in large 3D volumes which can be obtained from a single image[18–20]. However, holographic techniques crucially rely on coherent light as they require interference between a so-called signal and a reference field to recover the important phase information[21,22]. Thus, for spontaneous Raman scattering, an incoherent signal, holography seems impossible at first glance. Indeed, it is highly nontrivial to generate a suitable reference, and holographic imaging of incoherent radiation has, therefore, remained a curiosity. One way to nevertheless obtain the desired phase information is to rely on self-interference phenomena, which are accessible via shearing interferometry, and which have recently successfully been applied in 3D imaging of fluorescent emitters down to the single molecule limit[23].

Here we, for the first time, show that holographic imaging of spontaneous Raman signals is possible. We simultaneously record the phase and the amplitude of wide-field images of multiple SERS nanoparticles, alongside their respective Raman spectra by coupling a Michelson interferometer with a shearing interferometer-based holographic microscope. Moreover, our work enables digital image propagation for 3D localization of multiple SERS nanoparticles, positioned at different z-positions, from a single image. This approach not only validates our proof-of-concept demonstrations, but furthermore enables spectral multiplexing and Raman-band specific image decomposition.

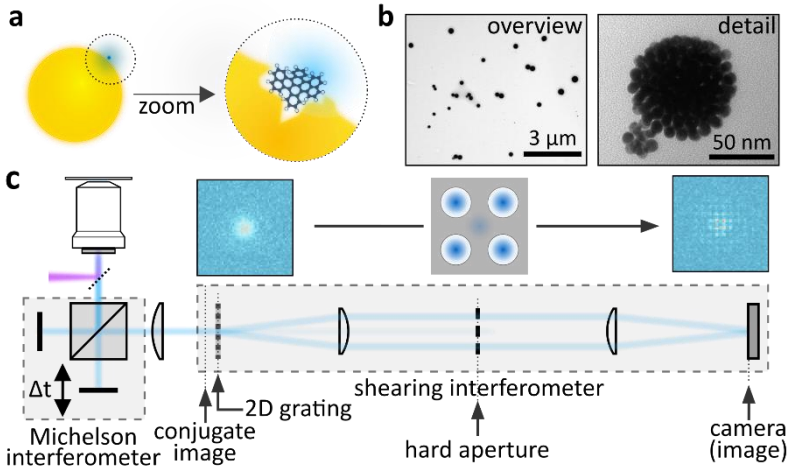

Figure 1: Bright SERS superclusters for spontaneous Raman holography. a) Localized hotspots and strong interactions between molecules and the SERS substrate give rise to considerably enhanced Raman signals. b) TEM overview image (left) alongside a detailed view (right) of one of the SERS encoded gold supercluster particles used in this study. c) Schematic of the spectrally resolved holographic widefield microscope composed of a Michelson and a shearing interferometer enabling simultaneously spectrally resolved imaging and image-phase measurements. The sample is widefield illuminated at 785 nm, using a fluence of 2.3 kW/cm^2, and the red-shifted SERS signal separated from residual laser light by means of a dichroic beamsplitter in combination with a longpass filter before entering the Michelson interferometer (see Supplementary Information for more detail).

For the preparation of suitable plasmonic material in terms of size SERS cross-section and intensity reproducibility, we synthetized highly homogeneous gold nanoparticles of 16 nm (Figure S1a), encoded with a variety of different SERS active molecules (Figure S2) and assembled them into

superclusters of around 100 nm (Figures 1b and S1a, b). These superclusters are characterized by a localized surface plasmon resonance (LSPR) with a maximum at 792 nm (Figure S1d) and enhancement factor of 2 x 10^6 as compared with the initial particles (see Supplementary Information). These bright and robust superclusters of nanoparticles with different SERS codes are an ideal system for fast multiplexed imaging, featuring reproducibility, easy preparation, colloidal stability and straightforward surface functionalization.

A microscope extended by a Raman shearing interferometer images the samples and allows accessing the complex electric field of widefield images of SERS emitters as well as their Raman spectra (Figure 1c). In brief, we focus a 785 nm laser into the microscope's back-focal-plane thus widefield illuminating the sample consisting of the previously mentioned nanoparticles doped with mercaptobenzoic acid (MBA). The red-shifted Raman signal is collected by the objective lens (UPlanS APO 60x, NA=1.2, Olympus) and separated from residual Rayleigh scattering with an 808 nm longpass filter (Semrock) before being imaged onto a 2D sCMOS-camera (ORCA-Flash 4.0, Hamamatsu). A Michelson interferometer equipped with a linear-actuator (M-230.10, PI), placed between the microscope objective and the imaging-lens, serves as a Fourier-transform spectrometer that directly accesses the frequency content of the radiation emitted from the particles (see Supplementary Information). To measure the phase and the amplitude of the widefield images we, furthermore, employ a 2D 0-π transmission phase-grating (Supplementary Information) that is relay imaged onto the camera[24,25]. Slightly offsetting the grating with respect to the intermediate image plane allows directly determining the images' phase-gradients as we will discuss in detail later.

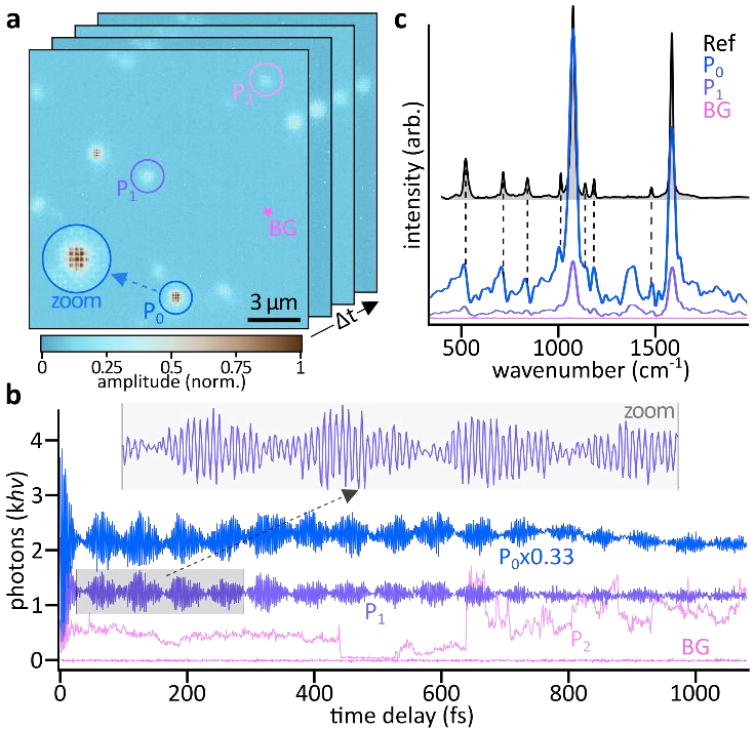

Figure 2: Wide-field time-domain SERS spectroscopy. a) Stack of SERS images recorded by varying the time-delay in one arm of the Michelson-interferometer. Several emission sites alongside a background-region are highlighted. The real-space image is plotted on an amplitude scale (square-root of the recorded intensity) for representation purposes only. b) Time-delay dependent integrated emission intensity of the respective regions highlighted in (a). The images are recorded by changing the time-delay in one arm of the Michelson interferometer, the overall setup is otherwise as outlined in Figure 1c c) Raman spectra obtained by discrete

Fourier-transformation of the data shown in (b). An ensemble reference spectrum recorded on a conventional Raman spectrometer (black) is shown for comparison.

Figure 2a shows a representative SERS particle-image where the individual point-spread-functions (PSFs) are reminiscent of sub-diffraction-limited emitters with the characteristic checkerboard pattern due to the 0-π phase-grating induced self-interference[23]. The pronounced amplitude-heterogeneity between individual particles is most likely caused by the strong SERS-signal dependence on the precise positioning of individual molecules in the plasmonic hotspots of the metallic nanoparticles[26,27]. To verify that the observed signal is indeed Raman scattering and not due to particle luminescence we record image-stacks while varying the length of one arm in the Michelson interferometer (Figure 2a). The delay-dependent integrated signal-intensity of most emission-sites exhibits the expected interferometric fringes with pronounced beating patterns reminiscent of spectral signatures with multiple frequency components (Figure 2b). Overall, the emission-intensity of most of the particles is extremely stable, and often constant over tens of minutes to hours, without signs of blinking or photobleaching. However, some particles show dramatic emission instabilities, reminiscent of single-molecule behaviour, which indicates that even the medium intensity SERS-emission might originate from individual molecules. To obtain single particle spectra we perform discrete Fourier transformations of the respective time-delay traces, results of which are shown in Figure 2c. These spectra show good quantitative agreement with an ensemble Raman-spectrum measured with a, conventional, Czerny–Turner spectrometer. We, furthermore, note that essentially the full emission-intensity is contained within the Raman bands with negligible presence of broadband components, such as fluorescence, that might be present for poorly-coupled, and hence unquenched, molecules.

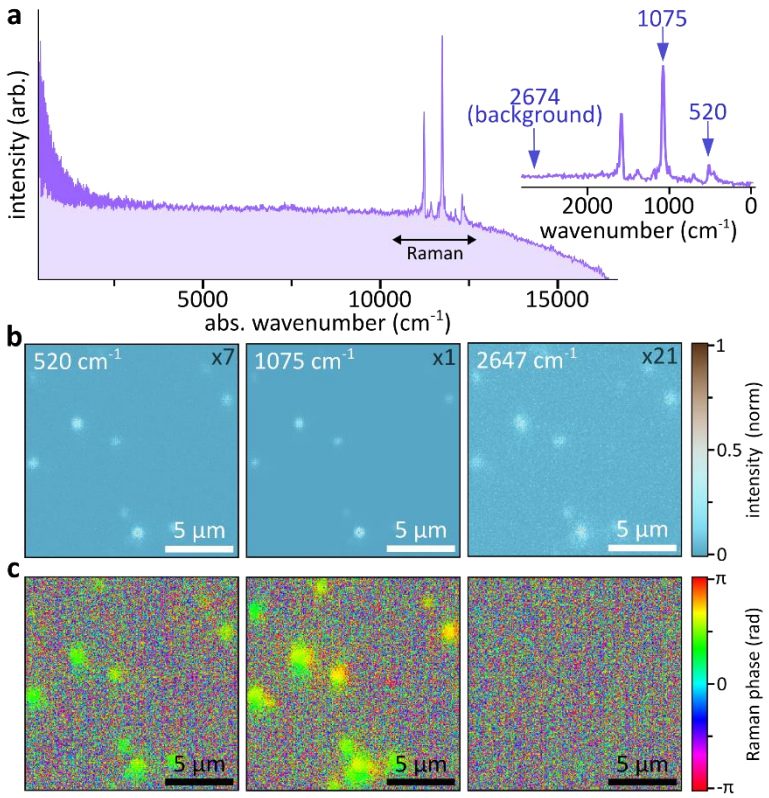

Figure 3, Spectral image multiplexing. a) Fourier transformation of a recorded SERS image interferogram alongside a magnification of the spectral Raman window. The reduced noise at high wavenumbers is most likely due to the step-size correction-algorithm of the Michelson interferometer which relies on interpolation of adjacent time-points thus artificial apodizing values close to Nyquist. b) Fourier-filtered radius-images obtained

by plotting the intensity for three different spectral bands. The black numbers indicate the relative intensity scaling factors. c) Corresponding phase of the spectral Raman bands. Note that the background shows no phase response.

After verifying the SERS-nature of the signal we will now attempt spectral decomposition of the single-color image into individual spectral bands. Figure 3a shows the spectral content of the entire image-stack, obtained analogous to Figure 2c but by summing the Fourier transformation of all camera-pixels. As expected, the particles' Raman spectrum is visible on top of a residual background caused by experimental noise such as stochastic emission-fluctuations and shot-noise. Based on the spectrum we select three spectral bands at 520, 1075 and 2674 cm^{-1}, respectively. The former two bands, which we formally assign to being due to CH-bending and ring-breathing modes of the adsorbed molecules, serve as references for weak and strong Raman signals and the latter as an estimate for background-induced signal. At each image pixel we Fourier filter the spectrum with a 17.7 cm^{-1} hard-aperture bandpass centred at the wavenumbers of interest and extract the amplitude of the inverse Fourier transformation to yield the multiplexed images (Figure 3b). As all SERS-particles are doped with the same molecules the decomposed images qualitatively agree with the spectrally integrated version shown in Figure 2a albeit some intensity differences between spectral bands. Surprisingly, the 2674 cm^{-1} image shows the presence of all particles, albeit at a drastically reduced intensity, even though no Raman-signal is present in the averaged spectrum (Figure 3a,b).

To rationalize this observation, we examine the phase term of the inverse Fourier transformation (Figure 3c). Here, only the spectrally observable bands at 520 and 1075 cm^{-1} show a distinct Raman-phase signal, with minor deviations from zero phase for all particles, which is due to a minor misalignment of the Michelson interferometer, resulting in a pathlength differences of ~100 nm across the image. The absence of a well-defined phase signal in the 2647 cm^{-1} image suggest that the amplitude observed is merely due to the increased total photon number detected at the locations of individual emitters. Here, shot-noise results in a spectrally uniform noise-increase that reflects itself in an apparent signal in the amplitude-term of the complex signal which is, by definition, positive: $A = \sqrt{x^2 + y^2}$. The Raman-phase-term, however, fluctuates freely and no signal is observed which serves as a robust guide for discriminating Raman emission in a specific wavenumber range from shot-noise induced signals due to Raman signals being present in a different part of the spectrum.

Following the spectral analysis of the SERS images we now turn our attention towards the shearing-interferometer that enables phase-measurements of the image. Importantly, we would like to stress that the Raman-phase discussed until now is distinctly different from the phase of the image which we are going to discuss in the following paragraphs. The former is solely determined by the time-delay in the Michelson interferometer while the latter contains information about the propagating electric field of the sample or, in other words, the image formation process. Deliberately different image-colour schemes are therefore used for the representation of the respective data.

As mentioned previously, the slightly offset 2D 0-π phase grating (Figure 1c) allows indirect determination of the phase of an image in a single shot[25]. As the wavefront passes the grating four identical image copies are generated as the first diffraction orders (+1/+1, +1/-1, -1/+1, -1/-1). These copies exhibit distinctly different k-vectors and a relay imaging-system recombines the diffraction orders on a camera where self-interference takes place[24,28]. As the grating is offset with respect to the relay-imaged conjugate image-plane the spatial overlap of the images is a function of the grating position (Figure 4a). If we consider a slightly out-of-focus emission site with spherical phase it becomes

apparent that the grating induced image-displacement directly translates into a phase-gradient measurement (Figure 4b). If the image-copies are not displaced identical parts of the image interfere and all phase information is lost. However, as soon as a shift is introduced different parts start interfering and the resulting phase-difference resembles a linear function with non-zero slope which is equivalent to the derivative of the spherical phase $\varphi(x,y) = (x^2 + y^2)$ we assumed previously. As the grating-generates several diffraction orders displaced in both x- and y-dimensions simultaneous gradient-measurements in both dimensions are performed.

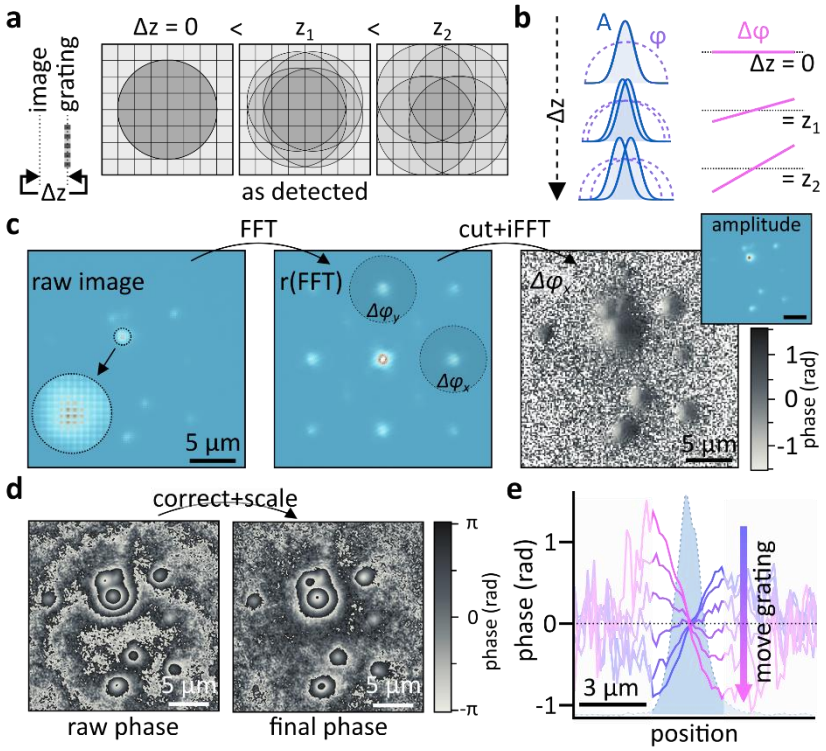

Figure 4, Extracting spatial phase information from Raman-images. a) PSF displacements as recorded on the camera depending on the offset of the 2D grating with respect to the conjugate image plane in the shearing interferometer. The further the grating is separated from the conjugate image plane the larger the separation between the individual diffraction orders on the camera. b) Phase-gradient scaling due to PSF displacements explained by considering a defocused emitter with resulting spherical phase. Blue: field amplitude, purple: phase, pink phase-derivative. c) Schematic of the steps necessary for phase-gradient extraction from an image recorded with the shearing interferometer. d) Raw phase image obtained from a) by 2D integration. The final phase is obtained by scaling, to account for the 2D-grating position, and removal of residual aberrations. e) Phase gradients $\Delta\varphi_x$ for multiple 2D-grating to conjugate image plane distances (lines) measured across a slightly defocused SERS emitting particle (light blue). The grating is moved by 200 µm between individual measurements.

To isolate the gradients we rely on the k-vector induced information-shift of the interference terms which we isolate in k-space via simple Fourier filtering[29]. The isolation-workflow is schematically outlined in Figure 4c. We Fourier transform the raw image which yields a k-space image consisting of the DC term alongside interference terms at different spatial frequencies. We isolate the terms containing either x- or y-direction gradients, $\Delta\varphi_x$ and $\Delta\varphi_y$, by multiplication with a circular hard-aperture followed by shifting to DC. Inverse Fourier transformation yields the phase-gradient as well as the amplitude in the respective dimensions (Figure 4c).

The images' phase is retrieved by means of a modified spiral phase integration algorithm which combines $\Delta\varphi_x$ and $\Delta\varphi_y$ (Figure 4d, see Supplementary Information for the integration-code)[30,31]. As the phase-gradients are strongly dependent on the distance between grating and conjugate image plane (Figure 4e), scaling and removal of potentially present residual background-phases is necessary before the final phase-image is obtained (Figure 4d, Supplementary Information).

Having analysed the spectral information as well as the image phase and amplitude we conclude with a "proof-of-concept" experiment, employing two kinds of SERS particles which are doped with different dye-molecules and then immobilized in a 3D-PVA matrix obtained by drop-casting and drying of an 8% aqueous PVA solution. Figure 5a shows a representative image on a logarithmic scale to account for the strongly varying emission intensities. As previously, we determine the spectra of individual particles which exhibit distinctly different Raman activity around 1006 cm^{-1} (Figure 5b), an observation that is also reproduced in spectrally decomposed images (Figure 5c), a multiplexing advantage that makes our approach an attractive contender for SERS imaging in general (Supplementary Information).

After Fourier filtering and gradient-based phase-integration we obtain the respective amplitude and phase images. A direct comparison between the images reveals particles with almost identical PSFs but very different phase values, reminiscent of concave and convex areas (Figure 5d). To understand these observations, we examine the phase-profile along the path shown in Figure 5d. Here, two adjacent emitters exhibit essentially inverted phase-terms (Figure 5e). This situation can be qualitatively understood by considering the wavefront of a focusing beam. Depending on the observer's position with respect to the focus the wavefront will appear as either being convex or concave. Translated to the image formation this observation is indicative of one particle being positioned below and another above the focal plane of the image.

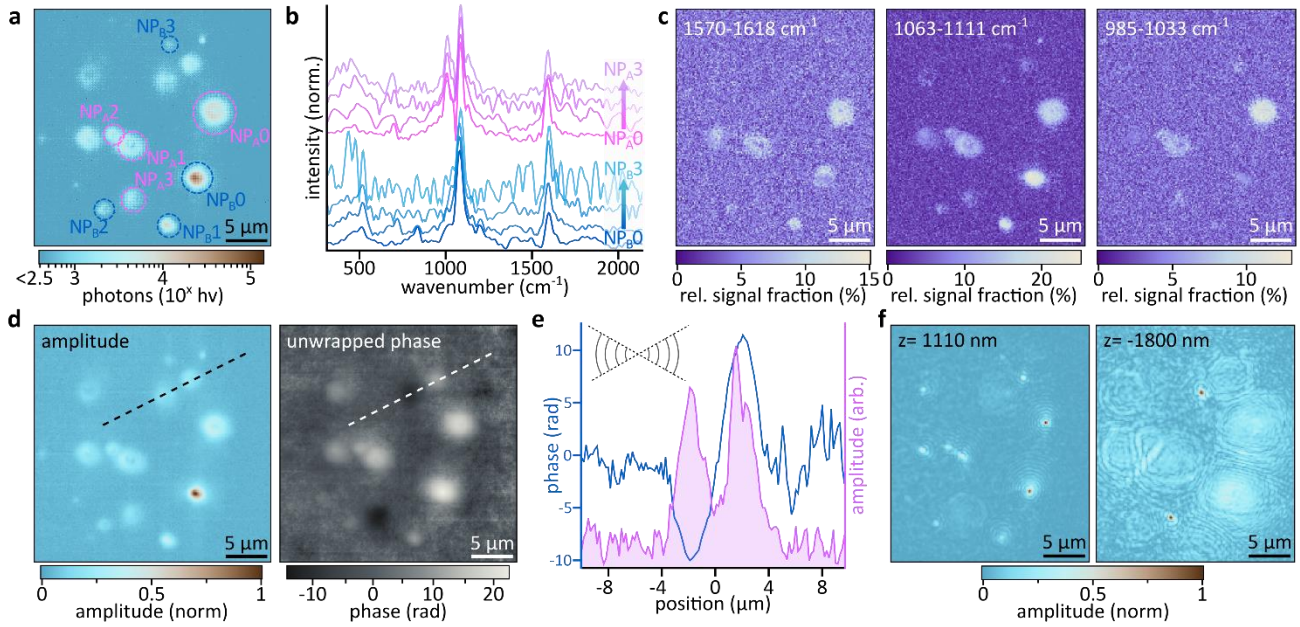

Figure 5, Multiplexed Raman phase-images. a) Logarithmic representation of a SERS image with differently doped particles (NP_A or NP_B) embedded in a 3D PVA matrix. b) Raman spectra of the indicated particles. c) Wavenumber-dependent spectral decomposition of the image shown in a). The spectral window exclusive to the NP_A particles clearly identifies the respective particle-fraction. d) Amplitude and phase images obtained from a) by means of Fourier-decomposition and 2D integration. e) Phase (blue) and amplitude (pink) of the cross-section indicated in d). The phases of the two particles show opposite curvature, indicative of one being located

below and the other above the focal plane as can be rationalized by imagining a wavefront around the focus of a laser beam (inset). f) Computational re-focusing of d) allows 3D particle localisation.

Beyond qualitative estimates of the relative z-position of individual emitters with respect to the focal-plane of the image it is furthermore possible to re-focus the entire image, at different z-positions, by relying on a suitable propagation kernel. Here, we propagate the complex NxN image to a new z-position by convolving with the following kernel:

$$K(x,y,z) = e^{-\left(iz\sqrt{k_m^2+k_x^2+k_y^2}\right)}$$

, with $(k_x, k_y) = \frac{2\pi}{n\Delta px\,(x,y)}$ for $\left(\frac{-N}{2} \le x,y < \frac{N}{2}\right)$ and $k_m = \frac{2n\pi}{\lambda}$ with *Δpx* being the magnified image-size corresponding to one camera pixel, *n* the refractive index and *λ* the signal wavelength. Based on this kernel we focus the images 1110 nm above and 1800 nm below the original image plane (Figure 5f) which shows that particles are indeed localized at different 3D locations within the PVA matrix. We, furthermore, verified that the particles are indeed present by manually re-focusing the images at the respective positions by moving the z-focus of the microscope by the distances mentioned above. For all propagations we assume a signal-wavelength of 860 nm which corresponds to 1193 cm^{-1}, close to the approximate wavenumber-mean of the Raman spectra of all observed particles (Figure 5e). Clearly, the SERS signals are not single-wavelength and nanometric miss-localizations might occur for propagation distances exceeding several wavelengths with the absolute error being directly related to the discrepancy between assumed and real mean-wavelength. Given the spectral agreement between individual particles such problems can, however, be corrected for by either computing the appropriate spectral mean or by 3D tracking the SERS particles in isotropic media and ensuring that the z-component of the estimated diffusion coefficient, which is solely determined by the quality of the computational propagation, matches the x- and y-components. Once determined the same particles can be used in the system of interest.

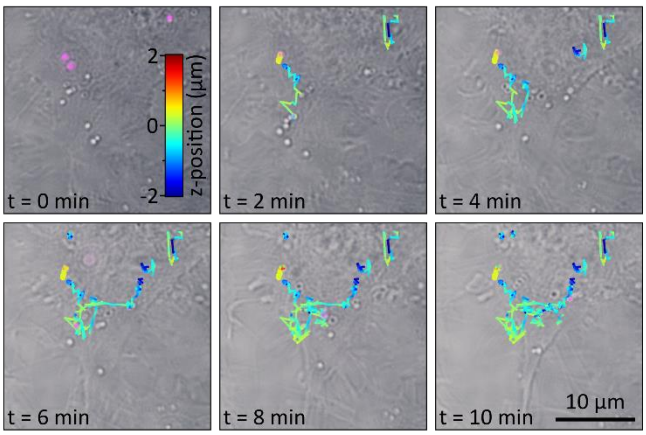

Figure 6, Live cell SERS particle tracking. The Raman signal (pink), recorded at a fluence of 1.8 kW/cm^2 and an integration time of 250 ms, is superimposed onto a brightfield image, recorded using Koehler illumination with a 470 nm fibre-coupled LED, of the cells. The trajectories of individual SERS particles are colour-coded to show the respective z-positions which are obtained by 3D localising the particles from image stacks generated via numerical propagation (Supplementary Information). 40 time-points are recorded per minute.

To conclude we present preliminary 3D holographic live cell tracking experiments (Figure 6). In brief, we incubate live HeLa cells with MBA-doped SERS superclusters for 3h at 37°C and then acquire time-lapse SERS as well as brightfield images to capture both the SERS particles' as well as the cells'

movements. Supplementary Video 1 shows a representative 10 min live-cell SERS-particle tracking video obtained by superimposing the aforementioned imaging channels, with minor displacement-differences between the two channels being due to the fact that brightfield and SERS images are acquired consecutively with a delay of 500 ms between acquisitions. To obtain the 3D trajectories of the individual SERS probes we perform Raman holography-based 3D single-particle localisation by relying on the propagation Kernel introduced above. Using the holographically measured amplitude and phase information of the SERS signal we generate 3D image stacks over a total z-range of $\pm 3\ \mu m$ by propagating in steps of 50 nm. Once obtained, we determine the precise 3D positions of all particles by a combination of Gaussian fitting and maximum-amplitude estimation (Supplementary Information). The individual particle positions are then linked[32] to generate the 3D trajectories shown in Figure 6 which show a combination of confined 3D diffusion with periods of active 3D transport within the live cell (Supplementary Video 1).

To summarize, we presented the first holographic measurements of spontaneous Raman images and, simultaneously, measured the spectral content of all individual SERS supercluster emitters. These experiments serve as proof-of-principle demonstrations and enabled the initial SERS-supercluster based live-cell tracking experiments. We demonstrated that the observed emission is indeed due to Raman scattering and not a result of background luminescence or poor filter choices. State-of-the-art Raman sensors for intracellular sensing mainly rely on the ratio of two distinct Raman bands and the simultaneous measurement of said bands can be implemented by spectrally manipulating some of the four diffraction orders generated by the 2D grating. Depending on its experimental implementation such strategies could allow simultaneously imaging up to six Raman bands for more complex multiplexing arrangements[33] which would allow complex chemical quantification of living systems in real time. A spectrally multiplexed implantation of single-shot Raman holography for chemical sensing inside living cells as well as of complex codes for anticounterfeiting applications, are currently being implemented and will ultimately enable precise 3D mapping of cellular activity with chemical sensitivity. We expect that such mapping capabilities will allow generating detailed chemical libraries of the metabolic processes in cells thus paving the way towards a better understanding of intracellular concentration equilibria and their dependence on cellular health. These observations will allow both detecting early stage infections and facilitate the discovery of novel cell-based therapies to fight recurrent malignancies such as cancer. Analogously, versatility and speed offered by the combination of superclusters and SERS holography opens the door for the generation of (and fast acquisition) of complex patterns with great technological applicability in fields such as the anticounterfeiting of money documents and commercial labels as it enables encoding spectral information in complex 3D patterns.

ACKNOWLEDGMENTS: Authors acknowledge support by the Ministry of Science, Innovation and Universities (MCIU/AEI: RTI2018-099957-J-I00 and PGC2018-096875-B-I00), the Ministry of Economy (MINECO: CTQ2017-88648-R, RYC-2015-19107 and "Severo Ochoa" program for Centers of Excellence in R&D SEV-2015-0522), the Catalan AGAUR (2017SGR1369), Fundació Privada Cellex, Fundació Privada Mir-Puig, the Generalitat de Catalunya through the CERCA program, and the Universitat Rovira i Virgili (FR 2019-B2). N.F.v.H. acknowledges the financial support by the European Commission (ERC Advanced Grant 670949-LightNet),

1. Albrecht, M. G. & Creighton, J. A. Anomalously Intense Raman Spectra of Pyridine at a Silver Electrode. *J. Am. Chem. Soc.* **4009**, 5215–5217 (1977).

2. Jeanmaire, D. L. & Duyne, R. P. Van. Surface Raman Spectroelectrochemistry Part1. Heterocyclic, Aromatic, and Aliphatic Amines Adsorbed on the Anodized Silver Electrode. *J. Electroanal. Chem.* **84**, 1–20 (1977).

3. Fleischmann, M., Hendra, P. J. & McQuillan, A. J. Raman Spectra of Pyridine Absorbed at a Silver Electrode. *Chem. Phys. Lett.* **26**, 163–166 (1974).

4. Langer, J. *et al.* Present and Future of Surface Enhanced Raman Scattering. *ACS Nano* (2019). doi:10.1021/acsnano.9b04224

5. Lane, L. A., Qian, X. & Nie, S. SERS Nanoparticles in Medicine: From Label-Free Detection to Spectroscopic Tagging. *Chem. Rev.* **115**, 10489–10529 (2015).

6. Wang, Y., Yan, B. & Chen, L. SERS Tags: Novel optical nanoprobes for bioanalysis. *Chem. Rev.* **113**, 1391–1428 (2013).

7. Zhang, X., Young, M. A., Lyandres, O. & Van Duyne, R. P. Rapid detection of an anthrax biomarker by surface-enhanced Raman spectroscopy. *J. Am. Chem. Soc.* **127**, 4484–4489 (2005).

8. Grubisha, D. S., Lipert, R. J., Park, H.-Y., Driskell, J. & Porter, M. D. Femtomolar Detection of Prostate-Specific Antigen: An Immunoassay Based on Surface-Enhanced Raman Scattering and Immunogold Labels. *Anal. Chem.* **75**, 5936–5943 (2003).

9. Pazos, E. *et al.* Surface-Enhanced Raman Scattering Surface Selection Rules for the Proteomic Liquid Biopsy in Real Samples: Efficient Detection of the Oncoprotein c-MYC. *J. Am. Chem. Soc.* **138**, 14206–14209 (2016).

10. Li, J. F. *et al.* Shell-isolated nanoparticle-enhanced Raman spectroscopy. *Nature* **464**, 392–395 (2010).

11. Dasary, S. S. R., Singh, A. K., Senapati, D., Yu, H. & Ray, P. C. Gold nanoparticle based label-free SERS probe for ultrasensitive and selective detection of trinitrotoluene. *J. Am. Chem. Soc.* **131**, 13806–13812 (2009).

12. Pazos-Perez, N. *et al.* Ultrasensitive multiplex optical quantification of bacteria in large samples of biofluids. *Sci. Rep.* **6**, 29014 (2016).

13. Pallaoro, A., Hoonejani, M. R., Braun, G. B., Meinhart, C. D. & Moskovits, M. Rapid identification by surface-enhanced raman spectroscopy of cancer cells at low concentrations flowing in a microfluidic channel. *ACS Nano* **9**, 4328–4336 (2015).

14. Palonpon, A. F. *et al.* Raman and SERS microscopy for molecular imaging of live cells. *Nat. Protoc.* **8**, 677–692 (2013).

15. Rivera-Gil, P. *et al.* Plasmonic nanoprobes for real-time optical monitoring of nitric oxide inside living cells. *Angew. Chem. Int. Ed.* **125**, 13939–13943 (2013).

16. Phan-Quang, G. C. *et al.* Three-Dimensional Surface-Enhanced Raman Scattering Platforms: Large-Scale Plasmonic Hotspots for New Applications in Sensing, Microreaction, and Data Storage. *Acc. Chem. Res.* **52**, 1844–1854 (2019).

17. Jiang, W., Kim, B. Y. S., Rutka, J. T. & Chan, W. C. W. Nanoparticle-mediated cellular response

is size-dependent. *Nat. Nanotechnol.* **3**, 145–150 (2008).

18. Latychevskaia, T. & Fink, H.-W. Holographic time-resolved particle tracking by means of three-dimensional volumetric deconvolution. *Opt. Express* **22**, 20994–21003 (2014).

19. Molaei, M. & Sheng, J. Imaging bacterial 3D motion using digital in-line holographic microscopy and correlation-based de-noising algorithm. *Opt. Express* **22**, 32119–32137 (2014).

20. Memmolo, P. *et al.* Recent advances in holographic 3D particle tracking. *Adv. Opt. Photonics* **7**, 713–755 (2015).

21. Gabor, D. A New Microscopic Principle. *Nature* **161**, 777–778 (1948).

22. Cuche, E., Marquet, P. & Depeursinge, C. Spatial filtering for zero-order and twin-image elimination in digital off-axis holography. *Appl. Opt.* **39**, 4070–4075 (2000).

23. Bon, P. *et al.* Self-interference 3D super-resolution microscopy for deep tissue investigations. *Nat. Methods* **15**, 449–454 (2018).

24. Patorski, K. The Self-Imaging Phenomenon and its Applications. *Prog. Opt.* **27**, 1–108 (1989).

25. Bon, P., Maucort, G., Wattellier, B. & Monneret, S. Quadriwave lateral shearing interferometry for quantitative phase microscopy of living cells. *Opt. Express* **17**, 13080–13094 (2009).

26. Camden, J. P. *et al.* Probing the structure of single-molecule surface-enhanced Raman scattering hot spots. *J. Am. Chem. Soc.* **130**, 12616–12617 (2008).

27. Michaels, A. M., Jiang, J. & Brus, L. Ag Nanocrystal Junctions as the Site for Surface-Enhanced Raman Scattering of Single Rhodamine 6G Molecules. *J. Phys. Chem. B* **104**, 11965–11971 (2000).

28. Maznev, A. A., Crimmins, T. F. & Nelson, K. A. How to make femtosecond pulses overlap. *Opt. Lett.* **23**, 1378–1380 (1998).

29. Takeda, M., Ina, H. & Kobayashi, S. Fourier-transform method of fringe-pattern analysis for computer-based topography and interferometry. *J. Opt. Soc. Am.* **72**, 156 (1982).

30. Arnison, M. R., Larkin, K. G., Sheppard, C. J. R., Smith, N. I. & Cogswell, C. J. Linear phase imaging using differential interference contrast microscopy. *J. Microsc.* **214**, 7–12 (2003).

31. Choi, I., Lee, K. & Park, Y. Compensation of aberration in quantitative phase imaging using lateral shifting and spiral phase integration. *Opt. Express* **25**, 30771 (2017).

32. Jaqaman, K. *et al.* Robust single-particle tracking in live-cell time-lapse sequences. *Nat. Methods* **5**, 695–702 (2008).

33. Rubin, M., Dardikman, G., Mirsky, S. K., Turko, N. A. & Shaked, N. T. Six-pack off-axis holography. *Opt. Lett.* **42**, 4611–4614 (2017).